Capabilities of through-the-substrate micro-diffraction: application of Patterson-function direct methods to synchrotron data from polished thin sections

Jordi Rius,[a]* Ana Labrador,[b] Anna Crespi,[a] Carlos Frontera,[a] Oriol Vallcorba[a] and Joan Carles Melgarejo[c]

[a]Institut de Ciencia de Materials de Barcelona, CSIC, Campus de la UAB, 08193 Bellaterra, Catalonia, Spain, [b]BM16-CRG Consorci Laboratori de Llum Sincrotró (LLS), c/o ESRF, F-38043 Grenoble, France, and [c]Departament de Cristal·lografia, Mineralogia i Dipòsits Minerals, Universitat de Barcelona, c/Martí-Franqués, Barcelona, Spain. E-mail: jordi.rius@icmab.es

Some theoretical and practical aspects of the application of transmission micro-diffraction (μXRD) to thin sections (≤ 30 μm thickness) of samples fixed or deposited on substrates are discussed. The principal characteristic of this technique is that the analysed micro-sized region of the thin section is illuminated through the substrate (tts-μXRD). Fields that can benefit from this are mineralogy, petrology and materials sciences since they often require *in situ* lateral studies to follow the evolution of crystalline phases or to determine new crystal structures in the case of phase transitions. The capability of tts-μXRD for performing structural studies with synchrotron radiation is shown by two examples. The first example is a test case in which tts-μXRD intensity data of pure aerinite are processed using Patterson-function direct methods to directly solve the crystal structure. In the second example, tts-μXRD is used to study the transformation of laumonite into a new aluminosilicate for which a crystal structure model is proposed.

Keywords: transmission microdiffraction; crystal structure; direct methods; polished thin sections; ilerdite.

1. Introduction

Polished thin sections of rocks with thicknesses up to 30 μm are commonly used in mineralogical and petrological studies. These sections are fixed on a glass substrate and are ideal for the microscopic observation and for determining the optical properties of the specimens under plane polarized transmitted light. These studies are normally complemented with SEM-BSE-EDS (SEM: scanning electron microscopy; BSE: back-scattered electron; EDS: energy-dispersive spectroscopy) images and analyses and, also, with electron microprobe analyses at selected points of the polished section. One advantage of this latter technique is that it can be applied to inhomogeneous samples owing to its local character. Very often, to complete the knowledge on a material, diffraction information of specific regions of the thin section is desirable. Such information can be obtained by performing the diffraction experiment in reflection mode, since the incoming beam does not pass through the substrate and hence no significant beam absorption takes place. Unfortunately, data reduction in this mode is hampered by the dependence of the gauge volume on the 2θ angle. Measurement in transmission mode,

i.e. by the beam passing through the thick glass substrate, is an alternative procedure that leaves the gauge volume unchanged during the experiment. A recent application of this procedure is described by Denecke *et al.* (2007). Diffraction in transmission mode greatly simplifies data reduction (Hammersley *et al.*, 1996); as a counterpart, it is affected by the strong beam attenuation caused by the thick glass substrate. This limitation can be overcome by using synchrotron radiation which combines high flux with a short wavelength. In the present contribution, various aspects of this specific transmission microdiffraction application, hereafter referred to as through-the-substrate microdiffraction (tts-μXRD), are analyzed. In particular, the evolution of line breadth with increasing Bragg angle is studied in detail. Line breadth affects peak overlap and hence the quality of the intensities derived from the powder diffraction patterns upon which the subsequent application of Patterson-function direct methods is based (Rius, 2011a). Application of direct methods is illustrated with data taken from two thin sections of aerinite-containing specimens [aerinite is a blue fibrous silicate pigment used in many Catalan Romanesque paintings between the XI and XV centuries (Rius *et al.*, 2004)]. From the

first thin section, diffraction data of pure aerinite are obtained and the viability of the technique is shown. Owing to the lateral resolution provided by the tts-μXRD technique, it can also be employed for studying structural aspects of intermediate phases at grain boundaries in solid-state reactions. This particular aspect is shown with the help of the second thin section (spot size is here 100 μm × 100 μm although it can be reduced depending on the beamline performance) where the transformation of laumontite into a previously unknown aluminosilicate is investigated.

2. Experimental

All the experiments were performed at the BM16-CRG beamline at the ESRF (Grenoble, France) (Juanhuix *et al.*, 2005). The principal optical elements of this line are a primary Rh-coated flat mirror limiting the energy range to 17 keV and producing vertical collimation, a Si(111) double-crystal monochromator and a secondary Rh-coated toroidal mirror focusing the monochromatic beam horizontally and vertically at the sample position. Data were collected on an ADSCQ210 flat CCD detector [210 mm × 210 mm, pixel size (2 × 2 hardware binned) p = 102.4 μm × 102.4 μm (horizontal × vertical)]. The spot size on the sample was controlled by two perpendicular pairs of tungsten slits. The sample arrangement is shown in Fig. 1.

The study of minerals on petrographic thin sections is a routine tool in many geological fields such as mineralogy, petrology, ore deposits and edaphology. A thin section is a thin slice of rock mounted on a glass slide. The first step in the preparation of the thin section is the impregnation of the rock with epoxy in order to ensure its consistence. Then the piece of rock is cut with an oil-cooled diamond saw to an approximately 2 × 4 × 1 cm parallelepiped which is fixed on a glass substrate with hard resin. The sample is progressively reduced with an abrasive grit until the sample surface is flat and finely
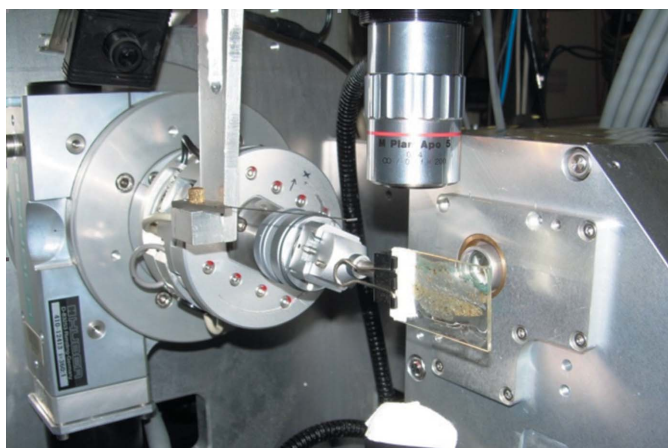
polished. Typical thicknesses of polished thin section and glass substrate are $t_S \simeq 30$ μm and $t_G \simeq 1.4$ mm, respectively.

First example. The viability of direct methods was studied on data from a thin section of an aerinite sample found near the Pantà de Canyelles (Lleida-Huesca, Spain). tts-μXRD patterns were measured at two different regions of the section, one containing pure aerinite (AE) and another with only glass contribution (G). The measurements are specified by AE or G followed by the sample-to-detector (q) distance in mm. Fig. 2 shows the typical aspect of tts-μXRD patterns collected on a flat CCD detector. Conversion of two-dimensional detector data of aerinite to a 2θ scan was performed with *Fit2D* software using LaB$_6$ as calibration standard (Hammersley *et al.*, 1996; Hammersley, 1998). *Fit2D* assigns the average value, $y = N_j^{-1}I(j)$, as the intensity for a radial bin at a given 2θ with bin width $\Delta 2\theta$ and where $N = (2\pi q/p)\tan 2\theta$ is the number of j
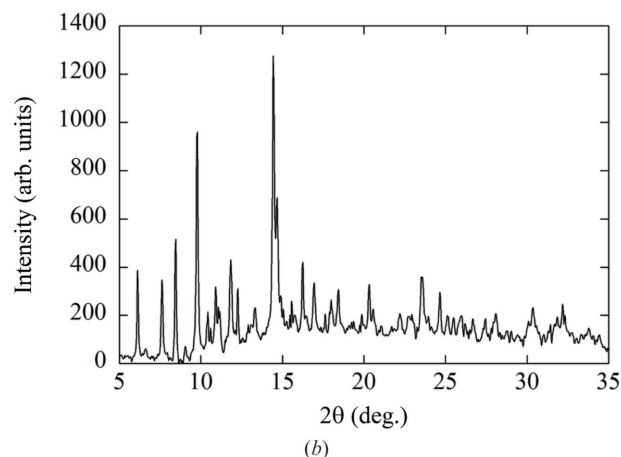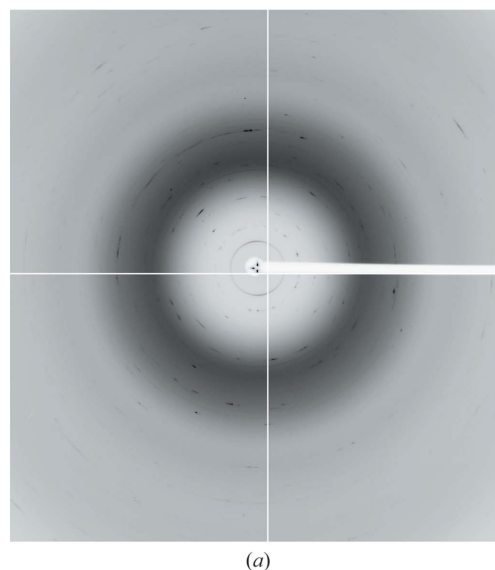

(a)

(b)

Figure 2
(a) Central portion of the tts-μXRD pattern ($d > 1.72$ Å) obtained by adding seven individual patterns of the ilerdite and aerinite mixture at different thin section regions (ilerdite: discontinuous Debye rings; aerinite: continuous ones). Data were collected on a flat CCD detector (exposure time: 60 s; sample-to-detector distance: 150 mm; λ = 0.7378 Å). (b) One-dimensional pattern obtained by circularly averaging the two-dimensional pattern in (a); for clarity, the glass contribution has been removed.

Figure 1
General view of the sample holder, motorized *XYZ*-stage with goniometric head, 12× video microscope and one-dimensional masking beam-stop (here positioned upwards out of the beam). To collect the two-dimensional XRD pattern, the sample is rotated by 90° around φ after positioning.

pixels with $2\theta(j)$ in the $[2\theta - (\Delta 2\theta)/2, 2\theta + (\Delta 2\theta)/2]$ interval (Vogel, 2010).

Two series of measurements were carried out using the following conditions:

(i) $\lambda = 0.9840$ Å ($\simeq 12.6$ keV): $q = 300$ mm, exposure time = 60 s, spot size = 250 × 220 µm. These conditions improve the instrumental resolution but reduce the measurable 2θ interval to $d_{min} = 2.15$ Å (equivalent to $2\theta_{max} = 42°$ for Cu $K\alpha_1$). These conditions are best suited for unit-cell indexing purposes. The 2θ range is 0.01–26.75° 2θ in 2048 equal steps ($\Delta\theta = 0.013°$).

(ii) $\lambda = 0.7378$ Å ($\simeq 16.8$ keV): $q = 150$ mm, exposure time = 300 s, spot size = 250 × 220 µm. The 2θ range is 0.01–45.19° 2θ in 2048 equal steps ($\Delta\theta = 0.022°$). These conditions allow atomic resolution ($d_{min} = 1.0$ Å) to be reached at the cost of slightly increasing the instrumental broadening. These data sets were processed with *DAJUST2* (Rius, 2010) to obtain the integrated intensities used by the Patterson-function direct-methods program *XLENS_PD6* (Rius, 2011b).

Second example. The second thin section studied corresponds to a sample from Tartareu (Lleida, Spain) (Rius *et al.*, 2009). Preliminary tts-µXRD patterns were measured at selected regions using the conditions fixed for the first example, *i.e.* $q = 150$ mm, $\lambda = 0.7378$ Å, exposure times between 30 and 60 s, calibration standard LaB$_6$. The only difference is the smaller spot size of 100 × 100 µm. In addition, microprobe analyses at different points were carried out to complement the microdiffraction information. These analyses were performed at the 'Centres Científics i Tecnològics' of the University of Barcelona. By combining the information of both techniques, the presence of K, Na-rich laumontite microcrystals, polycrystalline aerinite, a mixture of an unknown coarse-grained crystalline phase (hereafter provisionally called ilerdite from Ilerda, the Latin name for Lleida) with aerinite fibres inside, and finally a small amount of prehnite was confirmed (Fig. 3).
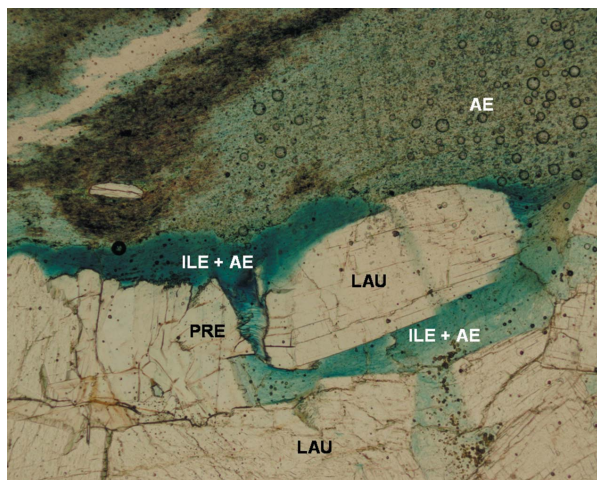

Figure 3
Photomicrograph of the polished thin section of the Tartareu specimen (transmitted polarized light, ~2.8 × 2.8 mm) (Rius *et al.*, 2009). The mineral association formed by laumontite (LAU), aerinite (AE), the mixture of ilerdite and aerinite fibres (ILE+AE) and a small amount of prehnite (PRE) are shown.

Table 1
Chemical composition of ilerdite.

(*a*) Composition of aerinite obtained by averaging 21 microprobe analyses (showing no significant dispersion). (*b*) Average composition of the mixture (ilerdite + aerinite) derived from 11 microprobe analyses of regions where microdiffraction measurements were performed. The fluctuation in composition is indicated by the e.s.d.s in parentheses. (*c*) Ilerdite composition by assuming that all Fe present in the mixture comes from aerinite. (*d*) Atomic proportions normalized to a total of eight Si and Al atoms in the unit cell (see text for the justification).

Element	Aerinite (wt%) (*a*)	Mixture (wt%) (*b*)	Ilerdite (wt%) (*c*)	Ilerdite (atomic proportion) (*d*)
Si	16.28	22.68 (1.00)	13.72	5.60
Al	7.06	9.53 (0.34)	5.64	2.40
Ca	7.72	7.39 (0.01)	3.15	0.91
K	0.02	0.69 (0.47)	0.68	0.20
Fe	7.68	4.22 (1.27)	0	
Mg	0.54	0.73 (0.07)	0.43	0.21
Na	0.24	0.06 (0.01)		
S	0.39	0.15 (0.07)		
O	31.93	39.35 (0.95)	22.22	15.93

The estimated chemical composition of ilerdite is given in Table 1. In order to find the crystal structure model for ilerdite, seven tts-µXRD patterns of the mixture at different regions on the thin section were collected. These seven patterns were added (Fig. 2a) and circularly averaged (Fig. 2b) to improve grain averaging.

3. The powder pattern of the sample

Application of the tts-µXRD technique requires measuring at least two diffraction patterns: one (T) with contributions from thin section and substrate (glass), and a second (G) with only the contribution from glass substrate. As shown in Fig. 4(*a*), the diffraction signal in T is significantly stronger than the statistical noise. For $\lambda = 0.7378$ Å, four well defined regions can be distinguished in T: (i) below 7°, where the pattern is dominated by the contribution of the phases of the thin section; (ii) between 7° and 16°, where the intensity reaches its maximum owing to the presence of the strong broad peak of glass and where the relative contribution of the thin section is small; (iii) between 17° and 31°, where the glass contribution remains approximately constant at one-third of the value reached at its maximum; (iv) above 31°, where the glass contribution steadily falls off.

The powder pattern (S) of the sample (*i.e.* of the gauge volume of the thin section) corresponds to the pattern difference T − kG, so that for $2\theta_i$

$$y_S(i) = y_T(i) - ky_G(i). \qquad (1)$$

For identical measurement conditions k should be slightly lower than unity owing to the small contribution of the hard resin used to fix the sample on the glass. For AE150, the resulting difference pattern (S) of the thin section is shown in Fig. 4(*b*). The weights used in the Rietveld refinements were $w(i) = 1/y_S(i)$ which worked well in all of the cases studied. In the literature, other weighting schemes can be found (Von Dreele, 2007; Chall *et al.*, 2000). The Rietveld refinements also
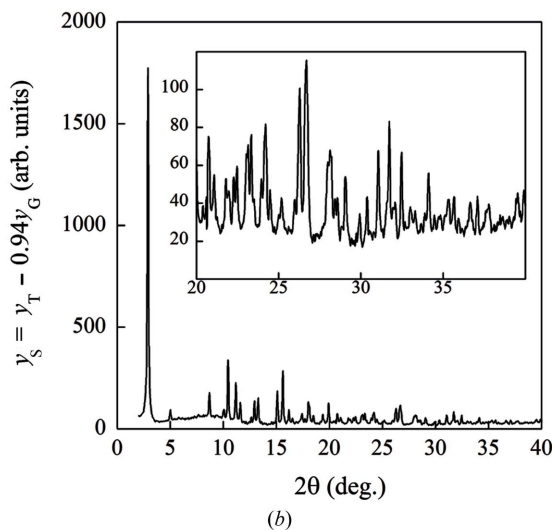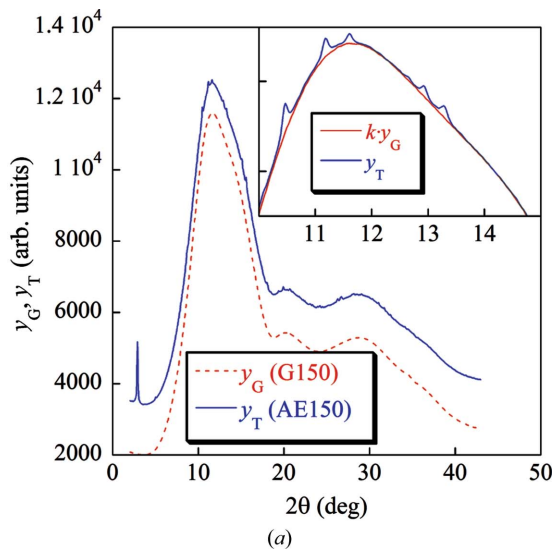
Figure 4
(a) Powder diffraction patterns T and G corresponding to AE150 (solid line) and to G150 (dashed line), respectively. T has contributions from thin section plus glass substrate, while G only from glass substrate. The AE150 pattern has been shifted up in the main panel. The inset shows ky_G ($k = 0.94$) and y_T around the maximum of y_G. (b) Plot of the difference powder pattern S ($y_S = y_T - 0.94y_G$) for AE150. The inset shows a zoom of the high-angle region.

need the estimation of the polarization and absorption factors. Regarding the former and for synchrotron radiation, the dependence of the P polarization factor on the ψ azimuthal angle, *i.e.* the angle between the normal to the polarization plane and the vector going from the centre of the two-dimensional detector to each particular pixel, is

$$P(2\theta, \psi) = \cos^2 \psi + \sin^2 \psi \cos^2(2\theta). \qquad (2)$$

Owing to the circular averaging, the average polarization factor is

$$\langle P(2\theta_i, \psi) \rangle_{\psi=0\,\text{to}\,2\pi} \simeq \frac{1}{2} + \frac{1}{2}\cos^2(2\theta_i). \qquad (3)$$

With respect to absorption, it is irrelevant since the sample is very thin [sample thickness (t) is around 30 μm]. If the linear

Table 2
Columns (a) and (b): FWHM (° 2θ) in AE150 and AE300 powder patterns measured at BM16; (c): contribution owing to sample broadening estimated from data collected at ID31 (ESRF) by assuming negligible instrumental broadening; (d) and (e): evolution of instrumental broadening for BM16 given by the divergence function δ(° 2θ) = $180° \cos^2(2\theta)(S_z + p)/2\pi q$ for $S_z = 0.220$ mm and $p = 0.100$ mm.

All breadths have been normalized to $\lambda = 0.7378$ Å to allow easy comparison.

Resolution d (Å)	AE150 FWHM (a)	AE300 FWHM (b)	AE_ID31 FWHM (c)	AE150 δ (d)	AE300 δ (e)
5.00	0.116	0.078	0.053	0.060	0.029
4.00	0.114	0.079	0.053	0.059	0.029
3.00	0.111	0.080	0.055	0.057	0.027
2.50	0.109	0.080	0.056	0.056	0.026
2.00	0.105	–	0.059	0.053	–
1.50	0.100	–	0.062	0.047	–
1.25	0.095	–	0.065	0.042	–
1.03	0.089	–	0.069	0.034	–

absorption coefficient of the thin section is μ_S, then, by introducing $u(2\theta) = (1/\cos 2\theta) - 1$, the absorption factor $A(2\theta)$ of the thin section for a parallel incoming beam (disregarding glass scattering) takes the form

$$A(2\theta) = \exp(-\mu_S t)\frac{1 - \exp[-\mu_S t\, u(2\theta)]}{\mu_S t\, u(2\theta)}$$
$$= \exp(-\mu_S t)\, Q(2\theta). \qquad (4)$$

In (4), $\exp(-\mu_S t)$ is constant for a given sample while $Q(2\theta)$ is unity for 2θ values close to zero and falls off more slowly for smaller $\mu_S t$. For both AE150 and AE300, respective $\mu_S t$ values are 0.0645 and 0.1673 with Q being 0.990 and 0.975 for $2\theta = 40°$.

4. Line broadening analysis

Ideally, crystal structure determination by direct methods requires almost complete data sets reaching atomic resolution. To see if direct methods can be applied to tts-μXRD data, line broadening in AE150 and AE300 powder patterns of aerinite are analysed and compared with the broadening observed in a synchrotron powder pattern of aerinite from Estopanyà (Huesca, Spain) which is known to be entirely dominated by sample broadening. This additional pattern was measured at the ID31 pattern ($\lambda = 0.5000$ Å) with the sample enclosed in a glass capillary (Ø = 1 mm) and with a battery of crystal analysers as secondary optics. Table 2 lists the experimental breadths at different d spacings, in which line breadths have been normalized to $\lambda = 0.7378$ Å in order to make comparison between patterns easier.

Since instrumental broadening is negligible in the ID31 pattern, line breadths in this pattern [column (c)] must be smaller than those in AE150 and AE300 [columns (a) and (b)]. The observed differences must principally reflect instrumental broadening. Compared with AE150, line breadths of AE300 are closer to those of ID31, so that instrumental contribution for AE300 is smaller than for AE150. Consequently, data measured at $q = 300$ mm (reaching $d_{min} = 2.15$ Å)

are more appropriate for unit-cell indexing. The evolution of instrumental broadening responds to the expected reduction of diffracted beam divergence with increasing 2θ according to

$$\delta(2\theta) = 180\cos^2(2\theta)(S_z + p)/(2\pi q). \qquad (5)$$

Columns (d) and (e) list $\delta(2\theta)$ values calculated for spot and pixel lengths equal to $S_z = 0.22$ mm and $p = 0.10$ mm. Inspection of these values clearly show that instrumental contribution becomes less important with increasing Bragg angle. This is favourable for the extraction of integrated intensities for direct methods. According to (5), to obtain a similar divergence as for AE300 with q fixed to 150 mm, $S_z + p$ must be halved, $i.e.$ $S_z \simeq 0.10$ mm and $p \simeq 0.05$ mm which represents a $16\times$ longer collection time. In practice, there is always a conflict between beam flux, spot size, pixel binning and collection time that depends on the characteristics of each particular beamline. In the direct-methods application to the unknown crystal structure (ilerdite), only the spot area was halved ($S_z = 0.10$ mm) owing to the limited flux available at 0.7378 Å.

5. Application of Patterson-function direct methods to tts-μXRD data

To be direct-methods successful, sufficient integrated intensities have to be extracted from the S pattern. The extraction procedure used in the present contribution is the cyclic alternate refinement of integrated intensities and profile parameters as described by LeBail et $al.$ (1988) [see LeBail (2005) for a retrospective]. The resulting integrated intensities are considered as resolved if all angular distances to the closest neighbouring reflections are greater than half the full width at half-maximum (FWHM). Unresolved reflections are grouped into clusters with a global integrated intensity. In the application of Patterson-function direct methods (Rius, 2011a) both individual and global integrated intensities are used. Notice that the model-free Rietveld refinement is not affected by sufficient grain averaging or by the presence of preferred orientation; consequently, the corresponding R_{wp} residual represents the lowest value which can be attained in the subsequent Rietveld refinement of the structure model.

5.1. Case 1: a single polycrystalline phase

In this section the applicability of direct methods to intensity data derived from the S powder pattern is checked. Integrated intensities were extracted from the AE150 measurement with $DAJUST2$ and corrected for Lorentz-polarization effects. Fig. 5 reproduces the final pattern matching. The difference profile is almost a flat line. To check the quality of the intensities, Patterson-function direct methods as implemented in $XLENS\_PD6$ were applied. The input unit-cell content was the true one and the intensity data were cut at $d_{min} = 1.10$ Å. The correct solution was found in 25 trials. Fig. 6 visualizes the structure model derived from the Fourier map of the highest-ranked solution which is almost identical to the published one (Rius et $al.$, 2004).
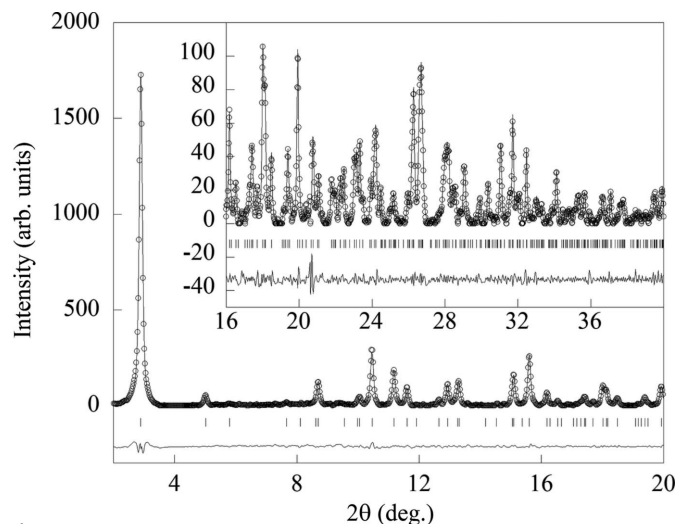

Figure 5
Full-pattern matching for the AE150 pattern of aerinite. Observed values are represented as circles. Solid lines correspond to the calculated pattern and the difference profile (bottom). Bragg reflections are represented as small vertical lines.

5.2. Case 2: a mixture of two crystalline phases

During the systematic microprobe analyses of some aerinite-containing thin sections, a deeper blue aerinite 'variety' with an abnormally high Si content [B1 and B2 phases in Rius et $al.$ (2009)] was observed. Since it was difficult to accommodate this extra Si content in the aerinite crystal structure, it was decided to carry out synchrotron microdiffraction experiments in order to shed some light. The tts-μXRD measurements showed that it was in reality a mixture consisting of a new crystalline phase (ilerdite) with aerinite fibres inside which were responsible for the blue colour (the presence of fibres was later confirmed by SEM). This mixture appears at the grain borders of laumontite and is most probably an alteration product of it (Fig. 3). Unlike aerinite, iler-
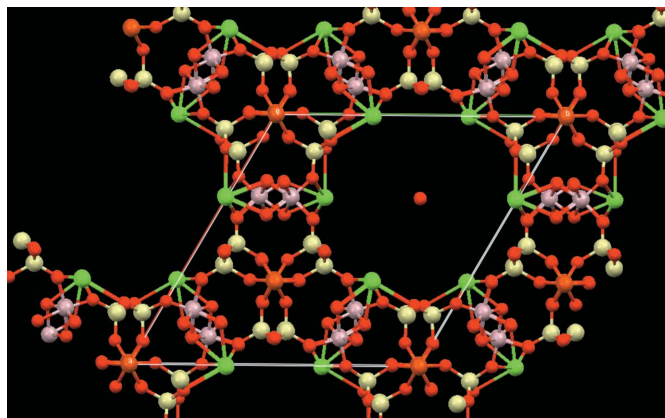

Figure 6
Application of Patterson-function direct methods to powder data of aerinite derived from tts-μXRD patterns measured at BM16. Crystal data of aerinite: $a = 16.9$, $c = 5.2$ Å; approximate unit-cell content: $Ca_5Fe_3Al_6[Si_{12}O_{36}(OH)_{12}]\cdot12H_2O$, $P3c1$. Inspection of the image, automatically generated from the Fourier map of the highest-ranked direct-methods solution, indicates that the model is essentially equivalent to that found by Rius et $al.$ (2004).
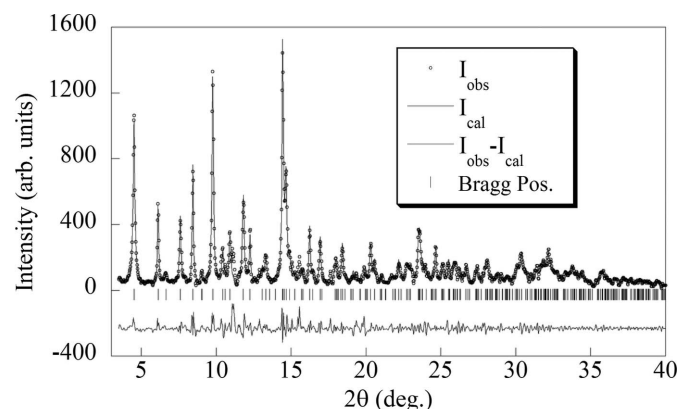
Figure 7
Whole-pattern matching of the powder pattern of ilerdite (obtained from the difference of mixture and aerinite patterns). Circles: observed values; solid lines: calculated pattern (top) and difference profile (bottom). Bragg reflections positions are indicated by small vertical lines.

dite is coarse-grained, so that only a few domains are illuminated (spot size is 100×100 µm). As already described in the experimental part, seven microdiffraction patterns of the mixture were taken at different locations of the grain borders, added and circularly averaged. Since the crystal structure of aerinite is known, its contribution could be subtracted from the pattern. This was done with the help of the *FullProf* suite of programs (Rodriguez-Carvajal, 1993; Roisnel & Rodriguez-Carvajal, 2000). The resulting difference pattern is the best approximation to the powder pattern of ilerdite. Indexing with program *DICVOL* (Boultif & Louër, 2004) gave a monoclinic unit cell. The refined cell parameters after whole-pattern matching with *DAJUST2* are $a = 6.398$ (1), $b = 6.904$ (1), $c = 9.427$ (1) Å, $\beta = 96.419$ (9)°, $V = 414$ Å^3 (Fig. 7). Peaks were fitted with pseudo-Voigt profiles and the refined FWHM of the individual Bragg peaks are between 0.11 and 0.12° 2θ. Figures of merit of the refinement are $R_{wp} = 0.144$, $R_p = 0.0907$ and $\chi^2 = 1.70$.

Application of Patterson-function direct methods to powder data requires, at least, the approximate unit-cell content. From Table 1 the approximate atomic proportions in ilerdite are known. On the other hand, the unit-cell volume of ilerdite (414 Å^3) is approximately one-third of the volume of laumontite, *i.e.* 1349 Å^3 for a unit-cell content equal to $Ca_4(Al_8Si_{16}O_{48})(H_2O)_{13.2}$ (Yakubovich & Simonov, 1985). By assuming that the metal content in the unit cell of ilerdite is one-third of that of laumontite and that the volume difference $[1349 - (3 \times 414)]/3 = 36$ is due to the loss of one water molecule ($\simeq 33$ Å^3), the unit-cell content of ilerdite should be close to $Ca_{1.33}(Al_{2.67}Si_{5.33}O_{16})\cdot 3.4H_2O$. This gives a total of eight Si and Al atoms in the unit cell. This value is used to scale the already known atomic proportions (Table 1), so that the resulting approximate unit-cell content of ilerdite should be $(Ca_{.9}Mg_{0.2}K_{0.2})(Al_{2.4}Si_{5.6}O_{15})(OH)_2\cdot nH_2O$ with $n \simeq 2$ [column (*d*)]. The chemical composition and the extracted intensities were introduced in *XLENS_PD6* (space group *Pm*; $d_{min} = 1.40$ Å; eight atoms sought in the unit cell). The best solution supplied the positions of the Si and Al atoms. Table 3 lists the positions found by direct methods and also their

Table 3
Peak positions of T and Al atoms as found by Patterson-function direct methods and after refinement from powder data (in italics) assuming *Pm* symmetry (unit-cell origin shifted to visualize the inversion centre of the ideal framework, *P2/m*).

The average composition of the six tetrahedrally coordinated T atoms in the unit cell, *i.e.* T1 (2×), T2 (2×), T3 (1×), T4 (1×), is close to $Si_{5.33}Al_{0.67}$.

Atom	x/a	x/a	y/b	y/b	z/c	z/c
T1	0.311	*0.309*	−0.297	*−0.284*	−0.093	*−0.126*
(T2)	−0.309	*−0.310*	0.289	*0.281*	0.092	*0.122*
T3	0.509	*0.495*	0	*0*	0.319	*0.325*
(T4)	−0.492	*−0.501*	0	*0*	−0.322	*−0.329*
Al5	0.091	*0.123*	0	*0*	0.119	*0.103*
(Al6)	−0.111	*−0.117*	0	*0*	−0.117	*−0.095*

values after a preliminary Rietveld refinement. The structural basic unit of the framework (Fig. 8) is a cage formed by double four-member rings (D4MR). These cages are joined by the Al corners giving rise to pentacoordinated Al atoms as shown in Fig. 10.

The missing Ca (K, Mg) atoms were located in a Fourier synthesis after optimizing the framework by restrained Rietveld refinements. Distances restraints (Å) were: T—O, 1.60 (2); O···O, 2.60 (10); Al5—O10 and Al6—O9, 1.65 (3); Al5—O(7) (2×) and Al6—O4 (2×), 1.71 (5); Al5—O4 (2×) and Al6—O7 (2×), 2.35 (8); O4—O4′, O7—O7′ and O4—O7, 2.35 (8). The scattering power at the Ca site was fixed at its expected value $[(0.45 \times 20) + (0.1 \times 12) + (0.1 \times 19) = 12.1$ electrons]. The O atoms (O11, O12, O13 and O14) around the Ca site were found with more difficulty and their occupancies globally refine to 1.00 (2). Final figures of merit are: $R_{wp} = 0.202$, $R_p = 0.157$, $\chi^2 = 2.52$ for 273 reflections. The observed and calculated powder patterns are shown in Fig. 9. The refined crystal structure model of ilerdite is listed in Table 4
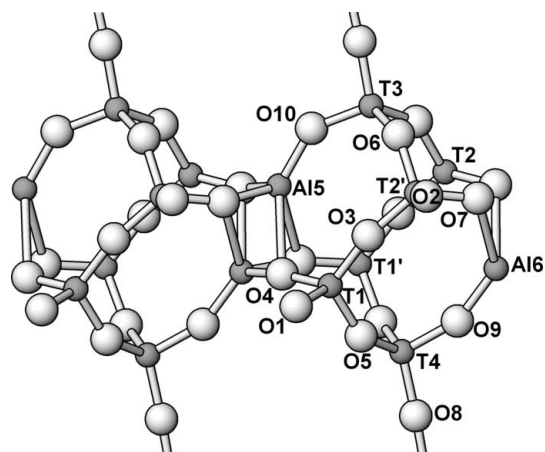

Figure 8
Perspective view with atom numbering of the D4MR cage of the ilerdite framework model (repeated along **a**) as obtained from Patterson-function direct methods and subsequent Rietveld refinement with only framework atoms. Noteworthy is the presence of pentacoordinated Al atoms at the cage junctions. The D4MR cages propagate along **b** *via* formation of four-membered rings with O1 and O2 as bridging O atoms. In the *c* direction O8 connects the T3 and T4 atoms of adjacent cages thereby spanning the framework reproduced in Fig. 10. T2 and T2′ are related by a mirror plane.
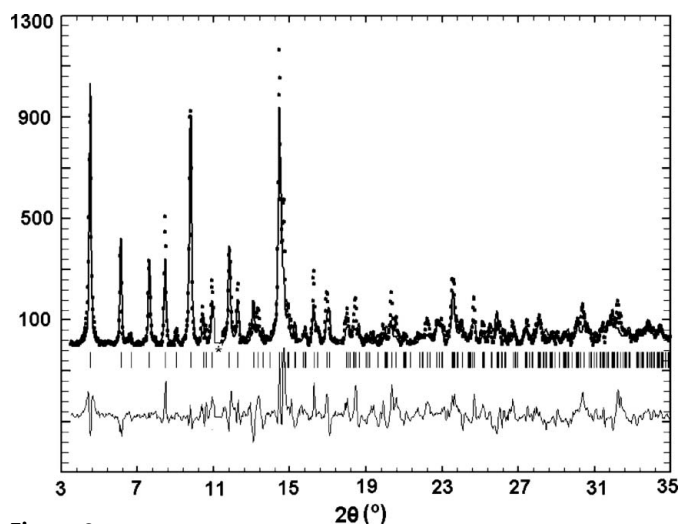
Table 4
Refined fractional coordinates for the ilerdite model.

Respective e.s.d.s for x, y, z are: 0.008, 0.004, 0.004 for T, Al and Ca atoms; 0.011, 0.006, 0.006 for framework O atoms; 0.02, 0, 0.015 for the rest of O atoms.

Atom/site	Atom type	Wyckoff site	x	y	z	Occupancy
T1	Si	2c	0.2652	0.2109	0.5497	1
T2	Si	2c	0.6630	0.2130	0.7858	1
T3	Si	1b	1/2	1/2	0	1
T4	Si	1b	0.4595	1/2	0.3453	1
Al5	Al	1b	0.0675	1/2	−0.1979	1
Al6	Al	1b	−0.1355	1/2	0.5721	1
O1	O	1a	0.1629	0	0.5183	1
O2	O	1a	0.7602	0	0.7980	1
O3	O	2c	0.4613	0.1860	0.6708	1
O4	O	2c	0.0689	0.3382	0.5860	1
O5	O	2c	0.3472	0.3137	0.4090	1
O6	O	2c	0.6110	0.3137	0.9355	1
O7	O	2c	0.8832	0.3235	0.7887	1
O8	O	1b	0.4701	1/2	0.1715	1
O9	O	1b	0.6986	1/2	0.4218	1
O10	O	1b	0.2547	1/2	−0.0608	1
Ca	Ca	2c	0.0101	0.1769	0.1167	0.605†
O11	O	1a	0.2473	0	0.2796	1.00 (2)
O12	O	1a	0.7420	0	0.1765	1.00 (2)
O13	O	1a	0.2523	0	−0.1470	1.00 (2)
O14	O	1b	−0.0387	1/2	0.2683	1.00 (2)

† The effective occupancy for the Ca site derived from the chemical composition (not refined).
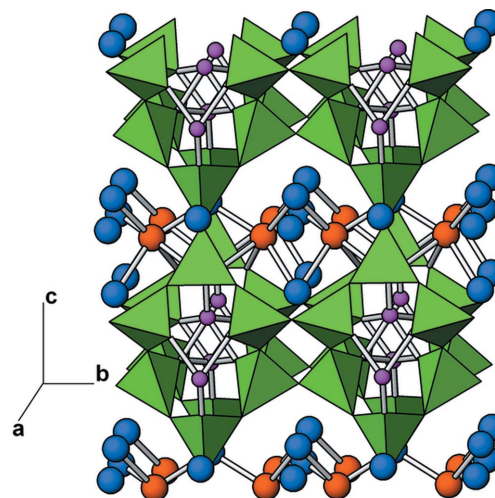

Figure 9
Final Rietveld refinement of the ilerdite model (Table 4). Circles: observed values; solid lines: calculated pattern (top) and difference profile (bottom). Bragg reflections positions are indicated by small vertical lines. The intensity is given in arbitrary units. The 2θ interval (11.0–11.4°) was excluded owing to the occasional presence of an unidentified impurity.

Figure 10
Perspective view of the framework model of ilerdite. Small circles: Al atoms; large circles: Ca (K, Mg) atoms and O atoms of hydroxyl groups or water molecules (yellow and blue, respectively, in online version).

polished thin sections have been measured. This was done at BM16 (ESRF, Grenoble) by using a ADSCQ210 flat CCD detector. To apply this technique, it is necessary to make measurements at two different regions, one containing the sample and the other with only the contribution from the sample holder (glass substrate) to properly subtract the glass contribution. It has been shown that the diffraction signal of these patterns is significantly stronger than the statistical noise and that the width of diffraction peaks is sufficiently small to permit confident estimates of the structure factors up to small d values ($\sim$1 Å). The usefulness of the resulting patterns has been checked by using the intensities extracted (by LeBail method) to reproduce, by applying Patterson-function direct methods, the structure of aerinite. The results obtained match very well with those of previous synchrotron powder diffraction measurements using the Debye–Scherrer configuration. Thus, it may be concluded that tts-µXRD can provide powder patterns of sufficient accuracy and resolution to solve complex crystal structures by direct methods on regions of about a hundred micrometres in size and even smaller. Another important advantage of this technique is its non-destructive character, as far as the sample must not be crushed or scraped. In a second step, tts-µXRD has been applied to obtain X-ray diffraction patterns from regions for which the composition (measured by microprobe) deviates significantly from that of aerinite. Detailed inspection of these patterns shows that in these regions aerinite coexists with a second previously unknown coarse-grained mineral phase that could be indexed reliably. Combination of multiple tts-µXRD data with Patterson-function direct methods allowed the crystal structure model for this new aluminosilicate 'ilerdite' to be derived.

and agrees with the expected unit-cell content, $(Ca_{0.9}Mg_{.2-}K_{0.2})(Al_{2.4}Si_{5.6}O_{15})(OH)_2 \cdot 2H_2O$. A perspective view of the model is reproduced in Fig. 10.

6. Conclusions

By means of the tts-µXRD technique, powder diffraction patterns of micro-sized selected regions on aerinite-containing

research papers

References

Boultif, A. & Louër, D. (2004). *J. Appl. Cryst.* **37**, 724–731.
Chall, M., Knorr, K., Ehm, L. & Depmeier, W. (2000). *High Press. Res.* **17**, 315–323.
Denecke, M. A., Somogyi, A., Janssens, K., Simon, R., Dardenne, K. & Noseck, U. (2007). *Microsc. Microanal.* **13**, 165–172.
Hammersley, A. P. (1998). *Fit2D. A 2-D Data Analysis Program*, http://www.esrf.fr/computing/scientific/FIT2D/.
Hammersley, A. P., Svensson, S. O., Hanfland, M., Fitch, A. N. & Häusermann, D. (1996). *High Press. Res.* **14**, 235–248.
Juanhuix, J., Labrador, A., Beltrán, D., Herranz, J. F., Carpentier, P. & Bordas, J. (2005). *Rev. Sci. Instrum.* **76**, 086103.
LeBail, A. (2005). *Powder Diffr.* **20**, 316–326.
LeBail, A., Duroy, H. & Fourquet, J. L. (1988). *Mater. Res. Bull.* **23**, 447–452.
Rius, J. (2010). *DAJUST2. A Program for Extracting Integrated Intensities from Powder Patterns.* Institut de Ciència de Materials de Barcelona, CSIC, Spain (http://www.icmab.es/xlens/).

Rius, J. (2011a). *Acta Cryst.* A**67**, 63–67.
Rius, J. (2011b). *XLENS_PD6. A Direct Methods Program for Solving Crystal Structures from Powder Diffraction Data.* Institut de Ciència de Materials de Barcelona, CSIC, Spain (http://www.icmab.es/xlens/).
Rius, J., Crespi, A., Roig, A. & Melgarejo, J. C. (2009). *Eur. J. Mineral.* **21**, 233–240.
Rius, J., Elkaim, E. & Torrelles, X. (2004). *Eur. J. Mineral.* **16**, 127–134.
Rodriguez-Carvajal, J. (1993). *Physica B*, **192**, 55.
Roisnel, T. & Rodriguez-Carvajal, J. (2000). *Mater. Sci. Forum*, **378–381**, 118–123.
Vogel, S. C. (2010). In *High-Pressure Crystallography: From Fundamental Phenomena to Technological Applications*, edited by E. Boldyreva and P. Dera. Dordrecht: Springer Science and Business Media.
Von Dreele, R. B. (2007). *J. Appl. Cryst.* **40**, 133–143.
Yakubovich, O. V. & Simonov, M. A. (1985). *Kristallografiya*, **30**, 1072–1076.